A high-impact *COL6A3* mutation alters the response of chondrocytes in neo-cartilage organoids to hyper-physiologic mechanical loading

Niek GC Bloks[1,*], Zainab Harissa[2,3,*], Shaunak S Adkar[2,3], Amanda R Dicks[2,3], Ghazaleh Hajmousa[1], Nancy Steward[2,3] Roman I. Koning[1], Aat Mulder[1], Berend B.R. de Koning[1], Margreet Kloppenburg[1], Rodrigo Coutinho de Almeida[1], Yolande FM Ramos[1], Farshid Guilak[2,3,†], Ingrid Meulenbelt[1,†].

[1]Leiden University Medical Center, Leiden, The Netherlands,

[2]Washington University, Saint Louis, MO, USA

[3]Shriners Hospitals for Children, Saint Louis, MO, USA

[*]*Shared first author*

[†]*Shared last author*

Abstract

Dysregulation of mechano-transduction via chondrocyte pericellular matrix (PCM) has been shown to induce osteoarthritis (OA), a highly prevalent degenerative disease of joint tissues. By performing exome sequencing in symptomatic OA patients, a high impact mutation in *COL6A3* encoding one of the monomeric sub-unit-3 of collagen type VI (COLVI) was identified. COLVI is an essential and specific protein functioning in the PCM. To study the downstream effects of the mutation in interaction with hyper-physiologic mechanical loading conditions, genetically *COL6A3*-edited human induced pluripotent stem cells (hiPSCs) were employed in our established

in-vitro cartilage organoid model. We showed mutated COLVI had significant lower binding to fibronectin (FN) and provoked an osteoarthritic chondrocyte state. Moreover, the *COL6A3* mutation abolished the initial stress responses of chondrocytes to hyper-physiological mechanical loading conditions. Together, the established sustainable cartilage organoid model provides unique opportunities to study the transduction of mechanical cues to chondrocytes and explore ways to counteract effects.Acquired insights could guide effective treatment development for OA.

Introduction

Osteoarthritis (OA) is a complex, multifactorial disease revolving around the interplay between genetic and environmental risk factors. In particular, biomechanical cues play a critical role in not only joint health but also drive the onset and progression of disease (*1*). Indeed, physiologic levels of mechanical loading by virtue of physical exercise can slow down OA disease progression (*2, 3*). In contrast, hyper-physiological loading, as seen with post-traumatic injuries such as articular fracture, meniscal tear, or rupture of the anterior cruciate ligament, concomitant with altered joint kinematics, is a major risk factor for the onset and progression of OA (*4*). Both physiological and hyper-physiological loading results in alterations in the structural composition of the cartilage extracellular matrix (*1*). These findings suggest that the balance of chondrocyte anabolic and catabolic processes for the maintenance of cartilage is tightly regulated by biomechanical cues.

Chondrocytes reside in a pericellular matrix (PCM), which modulates the transduction of mechanical cues from the extracellular matrix (ECM) towards the chondrocyte. The PCM for that matter contains specific proteins such as collagen 6 (COLVI) and fibronectin (FN) (*5*). In particular, collagen 6 (COLVI) is involved in regulating the mechanical properties of the PCM as well as calcium signaling in response to mechanical stress (*5-7*). Knock-out of a COLVI sub-unit, *COL6A1,* in a murine model induces an osteoarthritic phenotype through dysregulation of

44 mechano-transduction (*6, 8*). While loss of COLVI in humans is characterized by joint
45 contractures, hyperlaxity, and myopathy resulting in an inability to ambulate (*9*), the effect of
46 aberrant COLVI function on chondrogenesis and mechano-transduction remains unclear.
47 Here we report the identification of a *COL6A3* missense mutation through exome sequencing of
48 affected sibling pairs with generalized OA. *COL6A3,* coding for one of the monomeric sub-units
49 of COLVI (*10*) that resides in (*6*) and interacts with other PCM proteins (*11, 12*), is likely involved
50 in the regulation of cartilage structural composition and mechanical properties. We hypothesized
51 that the identified *COL6A3* mutation would perturb cartilage mechano-transduction in response to
52 hyper-physiologic loading, thereby contributing to OA pathogenesis. Recently, OA disease
53 modeling platforms utilizing human induced pluripotent stem cells (hiPSCs) have been used to
54 facilitate the interrogation of these pathogenic variants (*13*). To gain an understanding of the role
55 of COLVI in cartilage, we studied this mutation in an *in vitro* model of OA using hiPSC-derived
56 cartilage. We employed genetically *COL6A3*-edited hiPSCs to an established *in vitro* cartilage
57 organoid model, and these neo-cartilage organoids were exposed to hyper-physiological
58 mechanical loading conditions. The effects of the mutation on COLVI's interaction with other
59 PCM proteins was studied. To study the downstream effects of this mutation in response to hyper-
60 physiologic mechanical loading conditions, we characterized downstream molecular pathways
61 based on transcriptome wide profiles. Understanding the role of COLVI in the regulation of
62 mechanical stress will provide insight into etiology of OA and guide the development of effective
63 treatment strategies for OA.

64

65 **Results**

66 *Identification of a damaging mutation in COL6A3*

67 Whole exome-sequencing was applied to a Caucasian sib pair of Dutch ancestry at age of 61
68 affected predominantly with symptomatic OA at multiple sites (GARP study) (*14*). This resulted
69 in the detection of 81,416 genetic variants, after which a prioritization schema was followed to
70 identify pathogenic variants as previously described (*15*). In short, first, we selected novel variants
71 in in-house whole genome sequencing projects (N=222) and the BBMRI-Genome of the
72 Netherlands project (GoNL, N=473) (*15*). And second, damaging missense variants were selected
73 based on the prediction of sorting intolerant from tolerant (SIFT). This prioritization generated a
74 dataset of 38 novel coding variants that were predicted to have a functional impact on the protein
75 **(table S1)**. And third, these 38 novel coding variants were then further prioritized based on their
76 expression patterns in disease-relevant tissue by means of *in silico* analysis of 58 paired lesioned
77 and preserved samples, resulting in two genes that are highly expressed in cartilage and
78 differentially expressed between lesioned and preserved cartilage and bone; *MTHFR* (c.1667C>T,
79 p.Pro597Leu; cartilage: FC=0.84, FDR=0.04, bone: not detected) and *COL6A3* (c.4510C>T,
80 p.Arg1504Trp; cartilage: FC=1.75, FDR=2.25×10^{-5}, bone: FC=1.69, FDR=0.042) (*16*). *MTHFR*
81 encodes for methylenetetrahydrofolate reductase, which is involved in folate metabolism (*17*).
82 *COL6A3* encodes for collagen VI subunit A3, which together with collagen VI subunit A1 and A2
83 forms a triple helical COLVI, a primary component of the cartilage PCM, and interacts with other
84 proteins such as fibronectin and hyaluronan (*11, 12, 18*). The identified COL6A3 mutation is
85 located in the N-terminal VWA domains that are known to protrude away from the triple helical
86 structure. The *COL6A3* mutation was selected based on COLVI's role in regulating transduction
87 of mechanical cues in cartilage towards chondrocytes (*6*). To gain an understanding of aberrant
88 COLVI function in cartilage, we selected this high-impact mutation for studying its effects in 3D

89 in-*vitro* models of cartilage, and in interaction with hyper-physiological mechanical loading
90 conditions.

91

92 *Introducing the mutation in hiPSCs*

93 To investigate the effects of the aberrant COLVI on COLVI-mediated matrix deposition and
94 molecular pathways, a gene-edited human induced pluripotent stem cell (hiPSC)-derived neo-
95 cartilage organoid model was generated. We employed CRISPR-Cas9 single-stranded
96 oligonucleotide-mediated homology-directed repair in hiPSCs to attain biallelic modification of
97 rs144223596 (c.4510C>T) in an isogenic background, which was confirmed by Sanger sequencing
98 **(Fig. S1)**. Although there was a small C peak visible at rs144223596, this was considered noise,
99 and as such we considered the clone to be homozygous. Next, the *COL6A3*-edited and the unedited
100 isogenic control hiPSCs were differentiated into chondrocytes using a previously established
101 chondrogenic differentiation protocol (*19*). In short, hiPSCs followed a step-wise differentiation
102 protocol via mesodermal lineage differentiation towards chondroprogenitor cells (*19*). These cells
103 were then dissociated, and chondrogenesis was initiated in our organoid pellet model.

104

105 *Characterization of the matrix of isogenic control and COL6A3 mutant hiPSC-derived cartilage*
106 *organoids*

107 Successful differentiation towards chondrocytes and the production of neo-cartilage was
108 confirmed by protein staining of collagen II (COLII), collagen VI (COLVI), and sulfated
109 glycosaminoglycans (sGAGs) **(Fig. 1A)**. COLII and COLVI deposition was not affected by the
110 mutation as measured by staining intensity **(Fig. 1B)**. However, quantification of sGAG

111 deposition, using the dimethyl methylene blue (DMMB) assay normalized to DNA content,
112 showed a significant reduction in the COLVI-mutant compared to the isogenic control neo-
113 cartilage organoids (beta=0.55 ± 0.28, P=4.9x10^{-2}) **(Fig. 1C)**. Next, the isogenic and COLVI-
114 mutant neo-cartilage organoids were characterized by targeted gene expression analysis using RT-
115 qPCR of markers relevant for cartilage homeostasis and mechano-transduction **(table 1).** The
116 *COL6A3* mutation reduced expression of the catabolic marker *ADAMTS5*, while also reducing
117 expression of the anabolic markers *COL2A1* as well as *ACAN*.
118

119 *Transmission electron microscopy of the cartilage neo-matrix*

120 To further investigate the effect of the mutation on the structural properties of the PCM and ECM,
121 we performed transmission electron microscopy. As shown in **Figure 2A,** there was a reduced
122 abundance of GAG-like structures in the *COL6A3*-mutant neo-cartilage organoids versus the
123 isogenic control. Consistent with the DMMB assay, upon performing quantitative analysis of these
124 GAG-like structures using a deep learning algorithm, we confirmed that mutant COLVI cartilage
125 had significantly decreased aggregate size (Fig.2B; beta=-479.7, P=1.93X10^{-2}) and GAG
126 abundance (Fig. 2C; beta=-106.14 ± 14.95, P=2.52X10^{-6}).
127

128 *Binding of isogenic control and COL6A3 mutant COLVI to pericellular matrix proteins*

129 The identified R1504W mutation is located in the N-terminal domain of COL6A3 coding for a
130 von Willebrand Factor A domain, which is involved in binding two important proteins in cartilage
131 PCM and ECM, fibronectin and hyaluronan (*12, 13, 18*). Arginine at this position in the COL6A3
132 protein is evolutionary highly conserved, indicating that an amino acid change at this position is

133 likely to affect protein function **(Fig. S2)**. Thus, we hypothesized that the change from a polar
134 arginine to a non-polar tryptophan affects the interaction between COLVI and PCM/ECM proteins.
135 Hereto, we have performed a fibronectin and hyaluronan solid-phase binding assay with wild-type
136 and mutant COLVI, which was extracted from the chondrogenic differentiation medium of neo-
137 cartilage organoids. Results, as shown in Figure 2, demonstrated that binding to fibronectin was
138 reduced for mutant COLVI (beta=-0.13 ± 0.06, P=4.37 $x10^{-2}$). However, we could not detect any
139 binding of wild-type nor mutant COLVI to hyaluronan in our assay.

140

141 *Effect of missense COL6A3 mutation on the transcriptomic landscape*

142 Next, using RNA sequencing, we determined the downstream transcriptional effects of these
143 changes in the PCM and ECM related to the *COL6A3* mutation. The stranded RNA sequencing
144 allowed us to confirm the genotyping as performed with Sanger sequencing **(Fig S1)**, which
145 revealed the inclusion of both heterozygous (n=9) and homozygous (n=17) samples in our dataset
146 To avoid compromising on power in addition to detecting the most robust differentially expressed
147 genes (DEGs), we have pooled these heterozygous and homozygous samples after correction.
148 Multifactorial analysis revealed 3700 significant DEGs between the *COL6A3* mutant and isogenic
149 controls (FDR<0.05) **(Fig. 4A, table S2)**. Among these genes, 55% were upregulated and 45%
150 were downregulated. Notable highly significant DEGs were related to development and cartilage
151 metabolism, with the downregulation of structural PCM and ECM proteins, such as *COL27A1*
152 (FC=0.70, FDR=4x10^{-4}) and *PRG4* (FC=0.21, FDR=1.74x10^{-17}), increased catabolic activity, such
153 as *MMP9* (FC=3.67, FDR=7x10^{-16}), and ECM mineralization, such as *SPP1* (FC=2.7,
154 FDR=2.2x10^{-36}) **(Fig. 4A-B)**.

155 To determine the biological processes associated with the *COL6A3* mutation, we performed a
156 weighted gene co-expression network analysis (WGCNA) (*20*) on the RNA-sequencing data set.
157 This resulted in the detection of 20 distinct co-expression networks **(Fig. S3)**. Multifactorial
158 regression analysis revealed 10 co-expression networks with the first principal component
159 significantly associated with the *COL6A3* genotype **(Fig. S3)**. The top 3 most significant co-
160 expression networks associated with the *COL6A3*-mutant genotype were enriched for
161 developmental processes, cell-cell adhesion/anatomical structure morphogenesis, and ECM
162 organization **(Fig. 4C)**. Enrichment of ECM organization again underlines the detrimental effects
163 of the *COL6A3* mutation on the development of cartilage, affecting genes such as *LAMA5*, *LAMB2,*
164 and *COL18A1* that code for structural PCM components **(Fig. 4D)**. While enrichment of cell-cell
165 adhesion pathways suggests that the mutation also affects mechano-transduction via altered cell-
166 cell adhesion by downregulation of cadherin-associated genes**,** such as *CDH18*, *CDH6*, *PTGER4*,
167 *MAPK14,* and *ADAMTS5* **(Fig. S4)**. Of note is that *ADAMTS5* is downregulated in the *COL6A3*
168 mutant while quantification of sGAGs, the target peptides of ADAMTS5 cleavage, are reduced at
169 both the gene level (*ACAN*, **Table 1**) and protein level **(Fig. 1C; Fig. 3A-C).**
170 To study the relevance of the *COL6A3* mutation to OA pathophysiology, we determined the
171 overlap of gene expression between the effects of the *COL6A3* mutation and the differential
172 expression between lesioned and preserved cartilage from patient material collected post-joint
173 replacement surgery in a previously published dataset containing 58 paired samples (*16*) revealing
174 a subset of 582 overlapping DEGs **(table S4)**. We then performed pathway analysis on this subset
175 of genes **(Fig. 4B)**. The most significant enriched pathway was skeletal system development,
176 including transcription factors (*RUNX3*, *TNFRSF11B*), ECM components (such as *COL27A1*,
177 *COL11A2*), and anabolic factors (such as *IGF1*, *BMP3*). Well-known pathways related to

178 inflammation “inflammatory response” and “acute inflammatory response” were also enriched
179 containing inflammatory cytokines (IL31a) and general inflammatory response factors (*PTGES*,
180 *HLA-e*). Also, the “ossification” pathway was enriched, containing OA risk genes (*SPP1*, *TNC,*
181 and *MGP*). Genes related to cartilage metabolism were confirmed by quantitative reverse
182 transcription polymerase chain reaction (RT-qPCR) **(table S5).** Together, this data suggests that
183 the *COL6A3* mutation results in downstream expression changes, in part describing the
184 osteoarthritis pathophysiology.

185 Additionally, to explore the effect of the hetero- and homozygous *COL6A3*-mutated hiPSC-
186 derived neo-cartilage organoids, a dose-response effect was modeled for DEGs (FDR<0.05)
187 responding to the *COL6A3* mutation. To this end, the hetero- and homozygous *COL6A3* mutation
188 was considered as a covariate and analyzed for differential expression. This revealed a robust dose-
189 response effect (FDR<0.05) of the *COL6A3* mutation on gene expression in 2610 genes out of the
190 3700 DEGs affected by the mutation, **(table S6; Figure S6**), such as MMP9, PRG4, and SPP1
191 This dose-response effect further underlines the biological validity of the gene expression changes
192 due to *COL6A3* mutation.

193 Taken together, we showed that the *COL6A3* mutation reduces sGAG deposition **(Fig. 1)**, reduces
194 binding to fibronectin **(Fig. 2)**, and lowers the expression of mechano-sensor genes **(table 1)**
195 suggesting the mutation could affect the transduction of mechanical cues. Hence, we determined
196 whether the *COL6A3* mutation affects the transcriptomic response to hyper-physiologic
197 mechanical loading conditions. Hereto, two different organoid models were applied; cylindrical
198 constructs in which hiPSC-derived pellets were digested to obtain single-cell chondrocytes that
199 were then encapuslated in an agarose gelhydrogel, and spherical constructs with neo-cartilage
200 deposited by hiPSC-derived chondrocytes. Both these organoid models were exposed to hyper-

physiologic mechanical loading conditions [20% sinusoidal peak-to-peak strain at 5hz for 10 minutes]. Transcriptional activity was measured 12 hours after mechanical stimulation in isogenic controls (unloaded isogenic controls - n=13, mechanically stimulated isogenic controls - n=13) as well as *COL6A3*-mutant (unloaded *COL6A3* mutants – n=14 and mechanically loaded *COL6A3* mutants - n=12) organoids.

Effect of mechanical loading on the transcriptomic landscape

Next, we characterized the effect of hyper-physiologic loading conditions (*21*) on these neo-cartilage organoids. Multifactorial analyses revealed 177 DEGs (FDR<0.05) between unloaded and mechanically loaded organoids, of which 74% were upregulated and 26% were downregulated **(Fig.6A, table S7)**. Notable genes were, amongst others; *CD44* (FC=1.45, FDR=0.019), *CAV1* (FC=1.52, FDR=$4x10^{-4}$), *ITGA5* (FC=1.50, FDR=0.021); **Fig. 6B**), which are all genes encoding for mechano-sensors involved in OA pathophysiology.

To determine the biological processes affected by hyper-physiologic mechanical loading WGCNA co-expression networks were associated with mechanical loading, revealing 5 significantly associated co-expression networks **(Fig. S2; table S3)**. The top 3 most significantly associated modules were enriched for developmental and signaling processes, stress responses**,** and neuronal pathways **(Fig. 6B)**. While enrichment of signaling responses containing genes such as *IL1RL1* and *FOSL1* show an adaptive response to hyper-physiologic mechanical loading conditions **(Fig. 6D)**, enrichment of stress responses with genes such as *HSPA1B* and *DNAJA4* underlines the damaging effects of the hyper-physiologic mechanical loading conditions **(Fig 6E).**

223 *Effect of the COL6A3 missense mutation on the response to hyper-physiological mechanical*
224 *loading conditions*

225 Finally, the effects of the *COL6A3* mutation on the response to hyper-physiological mechanical
226 loading were investigated. To this end, a multifactorial analysis was performed resulting in a set
227 of 135 genes with a significant interaction effect (P<0.01) indicating that the mutation affected the
228 response to hyper-physiological mechanical loading **(table S8)**. Of these 135 genes, 70 proteins
229 show a significant protein-protein interaction (PPI) (FDR<0.05) as determined by STRING-DB
230 **(Fig. 7A)**. Notable is that highly connected genes in this PPI network such as; *PTGS2*, *IL1R1,*
231 *IRAK2, PECAM1,* and *ADAMTS5* are all related to catabolic and inflammatory signaling. *PTGS2*
232 is known to be regulated by TRPV4 signaling in response to mechanical stress (*22*) and is involved
233 in inducing an inflammatory response to stimuli (*23*). *IL1R1* codes for the receptor of interleukin-
234 1, one of the key inflammatory markers in OA, and thus is involved in inflammatory signaling,
235 while *IRAK2* encodes for the interleukin-1 receptor-associated kinase 2, which is involved in
236 interleukin-1 (IL-1) induced upregulation of NF-κβ (*24*). Upon performing stratified analysis, it
237 was shown that the interaction effect was particularly caused by an upregulation of gene expression
238 observed in isogenic controls in response to hyper-physiological loading conditions, that appeared
239 absent in the *COL6A3* mutant neo-cartilage organoids **(Figure 7B; table S9).**
240 To study the biological processes in which the response to hyper-physiological loading differed
241 between the isogenic control and the *COL6A3* mutants, associate this interaction effect with the
242 principal component of each detected co-expression network. This revealed three distinct co-
243 expression networks associated with the interaction effect, which were enriched for processes
244 related to signaling, ECM organization, and general biological processes **(Figure 7C)**. Enrichment
245 of pathways related to signaling shows an aberrant response in genes such as *INHBA* which acts

246 downstream of TRPV4 calcium channels (*22*), *CAV1*, *SEMA7A*, and *MMP3,* which are all genes
247 that respond to mechanical loading in isogenic controls, with an absent loading effect in the
248 *COL6A3* mutant **(table S3)**. Again, the enrichment of processes related to ECM formation and
249 organization, containing genes such as; *MMP13, RUNX1, FN1, LAMC1, EGFR,* and *PMEPA1*
250 **(Fig. 7D)**, underlines the effect of an impaired repair response to hyper-physiological mechanical
251 loading conditions in the *COL6A3* mutant. Also, the enrichment of general biological processes
252 including *IL1R1* highlights the aberrant response to mechanical loading in the *COL6A3* mutant
253 neo-cartilage organoids.

254

255 **Discussion**

256 In the current study, we identified a missense mutation in *COL6A3* (c.4510C>T, p.Arg1504Trp)
257 in a sibling pair of the GARP-study affected with symptomatic OA in two or more joint sites (*14*).
258 By introducing this high-impact mutation in hiPSCs using CRISPR-Cas9 genome engineering
259 while employing these cells in an established 3D *in vitro* neo-cartilage organoid model, we showed
260 that the mutation decreases cartilage matrix integrity **(Fig. 1C-D**), as reflected by a reduction in
261 abundance and size of GAGs **(Fig. 2A-C)**. Moreover, by subsequently isolating mutated COL6
262 protein, we showed that the mutation reduced binding to fibronectin **(Fig. 3)**. Analysis of the
263 transcriptome-wide gene expression changes with *COL6A3* mutation showed overlap with
264 transcriptomic changes due to OA-pathophysiology (*16*) **(Fig. 4)** indicating that an osteoarthritic
265 chondrocyte state appeared secondary to alterations in PCM function due to mutant *COL6A3.*
266 Finally, by exposing the neo-cartilage organoids to hyper-physiological mechanical stress, we
267 demonstrated that mutated *COL6A3* abolished the characteristic upregulation of inflammatory

signaling after mechanical loading (*21, 22, 25*) preceding the anabolic response in chondrocytes (*26, 27*). This was represented by inflammatory markers such as *IL1R1, PECAM1,* and *PTGS2*. In contrast, other catabolic genes such as *ADAMTS5*, normally being upregulated to hyper-physiologic mechanical loading conditions (*21*), did not respond to mechanical stress in the COLVI mutant neo-cartilage organoids. Taken together, these findings suggest that impaired binding between the PCM proteins COLVI and fibronectin resulted in a particular loss of proteoglycans, an OA chondrocyte disease state, and abolished the initial stress response to hyper-physiologic mechanical loading conditions.

Notably, we have explored the effects of the *COL6A3* mutation by challenging the neo-cartilage organoids with hyper-physiological mechanical loading conditions. Hereto, neo-cartilage organoids were exposed to 20% deformation at a rate of 5hz, based on previous research showing a loss of sGAGs, upregulation of catabolic genes, and downregulation of anabolic genes in response to these mechanical loading conditions (*21*). While we did not observe a statistically significant loss of sGAGs due to the short-term mechanical loading conditions used in this study **(Fig S6)**, we observed a marked upregulation of catabolic genes such as; ADAMTS1,3,5 degrading proteoglycans, MMP3,9 and 13 which degrade COLII fibrils, and MMP25 cleaving fibronectin **(table S9).** The fact that we did not observe a loss of sGAGs might be explained by a relatively lower sensitivity of detecting differential protein expression in comparison to differential gene expression, but also that protein and gene expression is measured at the same time, possibly explaining that there is not yet an observed loss of sGAGs or COLII in response to this catabolic gene-expression profile. However, this catabolic gene-expression profile is overlapping with a previously published dataset showing upregulation of catabolic genes as well as inflammatory markers in response to damaging mechanical stress in a human ex-vivo explant model (*28*).

291 By exposing the cartilage organoids to hyper-physiological mechanical stress to the cartilage
292 organoids, we demonstrated that mutated *COL6A3* abolished the characteristic inflammatory
293 response to hyper-physiological stress (*22*) which precedes regenerative anabolic signaling (*26*).
294 In line with previous experiments, we show that *PTGS2* and *PTGER4*, coding for prostaglandin
295 E2 synthase and the prostaglandin E2 receptor EP4 are upregulated to mechanical stress in the
296 isogenic control organoids while lacking response in the *COL6A3* mutant organoids **(table S9)**
297 (*22, 28, 29*). These PGE2-related genes such as *PTGES* and *PTGS2* were upregulated, similar to
298 OA pathophysiology. However, inhibiting COX2, upstream of PGE2 signaling only has modest
299 effects on pain and disability (*30*), in other tissues, such as epithelium the PGE2 – EP4 axis is
300 essential to initiate a repair in response to stressors (*31*). Also, the interleukin-1 signaling pathway
301 is affected by an ablated upregulation of *IL1R1* and its downstream kinase involved in NF-κβ
302 signaling, *IRAK2*, in response to mechanical loading, possibly explained by being upregulated in
303 the *COL6A3* mutant **(table S10)**. Moreover, matrix-degrading enzymes such as MMP13 and
304 ADAMTS5 which normally are upregulated in response to mechanical loading (*28, 32, 33*) both
305 showed an impaired response to mechanical stress in the *COL6A3* mutant. Of note is that
306 ADAMTS5, the main enzyme cleaving aggrecan, is downregulated in the *COL6A3* mutant, but
307 there is also a decrease in sGAG concentration in the neo-cartilage pellets. One explanation for
308 this opposing observation is that *ADAMTS5* gene expression could be upregulated during matrix
309 deposition in the formation of cartilage in the *COL6A3* mutant, but at the end of the differentiation
310 is down-regulated to attempt to rescue sGAG concentration. While it is tempting to pose that the
311 reduced binding of the mutant COLVI with fibronectin affects the transduction of mechanical cues
312 toward the chondrocytes, more research is needed to confirm this relationship. The fact that the
313 genes showing an interaction effect did not appear differentially expressed upon hyper-

314 physiological loading in the combined multifactor analysis can be explained by the interaction
315 effect masking the main effects of hyper-physiological loading. Henceforth, we have applied an
316 additional stratified analysis of the loading effect in the isogenic controls, showing that indeed
317 most of these genes respond to mechanical stress **(table S9)**, consistent with previously published
318 data describing the effects of mechanical loading on gene expression (*21, 22, 28*).
319 Here, we studied the effect of a high-impact *COL6A3* in hiPSC-derived neo-cartilage organoid
320 model that had been genome-edited via CRISPR-Cas9 to harbor this mutation. While we initially
321 concluded, based on sanger sequencing, that our hiPSCs were homozygous, genotyping utilizing
322 our RNA sequencing data showed that there were also heterozygous samples included. These
323 heterozygous *COL6A3* mutant cells could have arisen due to a selective advantage upon expanding
324 hiPSCs. Nonetheless, availability of hetero- and homozygous samples allowed us to study a
325 possible dose-response effect of the mutation on RNAseq data and confirmed a dose-response
326 effect in 2610 genes out of the 3700 DEGs. This adds to the validity of our data and biological
327 relevance of the studied *COL6A3* mutation, as there was an additive effect of the hetero- and
328 homozygous *COL6A3* mutants on DEGs such as SPP1, MMP9, and PGR4. **(table S6, Fig. S7)**.
329 We have applied both cylindrical disc-shaped organoids (*22*) as well as spherical pellets (*13, 21*).
330 The advantage of the first model is an ensured equal distribution of mechanical stress throughout
331 the disc-shaped sample. The advantage of the second model is that it allows harnessing the original
332 matrix deposited by the hiPSC-derived chondrocytes thereby permitting the characterization of
333 changes in the ECM. Combining all samples using multifactor analysis has allowed us to show
334 that indeed aberrant COLVI function exerts part of its deleterious effects via altered mechano-
335 transduction of mechanical cues. Additionally, this model of hyper-physiological loading in hiPSC
336 neo-cartilage organoids can be expanded to define and apply more beneficial mechanical loading

337 regimes, further unraveling the shift in molecular mechanisms underlying the normal physiological
338 response to loading that might further aid in the development of treatment strategies.
339 In contrast to previous findings (*12*), we could not detect any binding of COLVI with hyaluronan,
340 which might be explained by the source of the COLVI proteins, as they were extracted from the
341 culture medium. Alternatively, other intermediary proteins are necessary for binding COLVI to
342 hyaluronan which might not have been present in the medium (*11*). Moreover, we have used TEM
343 in combination with a, yet to be published, machine-learning tool to detect changes in GAG size
344 and abundance. The reliability of machine learning tools relies on prudent training of the machine
345 learning algorithm by correct labeling of the structures to be quantified. Here we relied on the
346 similarity with previously published data. Nevertheless, the reduced abundance of GAGs as
347 measured with TEM is in line with the results of the DMMB assay, as well as the Alcian blue
348 staining **(Fig. 1A-C; Fig. 2A-C)**.
349 By using genetic engineering of hiPSC-derived neo-cartilage organoids while implementing
350 hyper-physiological mechanical loading conditions, we are among the first to demonstrate that
351 aberrant function of COLVI in the PCM, abolishes the initial inflammatory response to hyper-
352 physiological loading, as marked by, amongst others, changes in *PTGS2* and *PGE4*. Moreover, we
353 showed that secondary to the COLVI mutation provoked alterations in PCM function,
354 chondrocytes appeared to enter an OA disease state. The established sustainable methodology
355 provides an unique framework to determine the role of proteins in the transduction of mechanical
356 cues from ECM to chondrocytes and to explore ways to modify and/or counteract them. Since
357 biomechanical cues play a critical role in joint health and disease acquired insights could
358 eventually contribute to discovery of effective treatment options for OA.

359

360 **Materials and Methods**

361 *Experimental design*

362 The objective of the current study was to study the effects of a likely causal pathogenic mutation,
363 thereby elucidating the effects of aberrant collagen VI functions. Exome sequencing was applied
364 to identify a pathogenic mutation. To study the underlying effect of this mutation, the mutation
365 was introduced in hiPSCs using CRISPR-Cas9 genome engineering, of which a neo-cartilage
366 model was created, followed by mechanical loading and functional analysis.

367

368 *Exome sequencing*

369 Exome sequencing of a sibling pair with generalized OA at multiple joint sites was performed by
370 Illumina HiSeq 2000 technology (Beijing Genome Institute). The sequences were generated as
371 100–base pair paired-end reads, after enrichment of 44-Mb exonic sequences by NimbleGen EZ
372 (Roche NimbleGen). Raw imaging files were processed by Illumina base calling software v1.7
373 with default parameters. SOAPaligner/SOAP2.21 was used to align reads to the GRCh37 reference
374 genome at the UCSC Genome Browser website (http://genome.ucsc.edu/) (*34*).

375

376 *hiPSC line and cell culture*

377 An hiPSC line as described earlier was used as the unedited isogenic control (*19*). In short, RVR-
378 iPSC line was retrovirally reprogrammed from BJ fibroblasts and characterized. The hiPSCs were
379 maintained under standard conditions (37 °C, 5% CO_2) on Matrigel (Corning) coated plates and

380 refreshed daily with TeSR-E8 medium (STEMCELL Technologies) upon reaching approximately
381 70% confluence.

382

383 *Genome editing of hiPSCs*

384 gRNA targeting *COL6A3* (5'-TCTGAAAACCTACAGATCCC -3') were complexed with Cas9
385 protein at 25 C for 10-15' and added to a RVR-hiPSC cell suspension of 500K cells in 400 µL
386 mTeSR to generate the edited hiPSCs. 500 pmol of ssODN (5'-
387 CTTGCCACAAATTCGAGAGCCTTGCCAGTG
388 TTCAGTGGGGACCCCCCTCTGAGCCTCAGGCGCCATATGGCGTCCAGCACCGGGGC
389 GTGGGATCTGTAGGTTTTCAGATAGAATTCTGGGAAGACAT-3') harboring the risk
390 variant was added to cell suspension. Cells were electroporated with BioRad Gene Pulser system
391 with the following conditions: [250 V, 750 µF, ∞ Ω, 0.4 cm]. Cells were plated at low density and
392 colonies were picked to obtain clones derived from single cells. As the risk variant created an
393 NDEI site, clones were screened by PCR amplification of the risk allele and digestion with NDEI
394 (New England Biolabs) in CutSmart Buffer for 1 hour at 37C. Successful editing of the targeted
395 variant was confirmed by Sanger sequencing **(Fig S1)**.

396

397 *hiPSC differentiation to induced chondrocytes*

398 Generation of induced chondroprogenitor cells (hiCPCs) was based on a protocol previously
399 described (*19*) which was shown to produce similar neo-cartilage to that produced by human
400 primary articular chondrocytes (*35*). When hiPSCs reached 60% confluence, the culture medium

401 was switched to mesodermal differentiation (MD) medium, composed of IMDM GlutaMAX
402 (IMDM; Thermo Fisher Scientific) and Ham's F12 Nutrient Mix (F12; Sigma-Aldrich) with 1%
403 chemically defined lipid concentrate (Gibco), 1% insulin/human transferrin/selenous (ITS+;
404 Corning), 0.5% penicillin-streptomycin (P/S; Gibco), and 450 μM 1-thioglycerol (Sigma-Aldrich).
405 Before induction of anterior primitive streak (day 0), hiPSCs were washed with wash medium
406 (IMDM/F12 and 0.5% P/S) and then fed with MD medium supplemented with activin A (30 ng/ml;
407 Stemgent), 4 μM CHIR99021 (CHIR; Stemgent), and human fibroblast growth factor (20 ng/ml;
408 FGF-2; R&D Systems) for 24 hours. Subsequently, the cells were washed again with wash
409 medium, and paraxial mesoderm was induced on day 1, by MD medium supplemented with 2 μM
410 SB-505124 (Tocris), 3 μM CHIR, FGF-2 (20 ng/ml), and 4 μM dorsomorphin (Tocris) for 24
411 hours. Before induction of early somite (day 2), cells were washed with wash medium, and then
412 cells were fed with MD medium supplemented with 2 μM SB-505124, 4 μM dorsomorphin, 1 μM
413 C59 (Cellagen Technology), and 500 nM PD173074 (Tocris) for 24 hours. Subsequently, cells
414 were washed with wash medium, and for induction of sclerotome, cells (days 3 to 5) were fed daily
415 with MD medium supplemented with 2 μM purmorphamine (Stemgent) and 1 μM C59. To induce
416 chondroprogenitor cells (days 6 to 14), cells were washed briefly with wash medium and fed daily
417 with MD medium supplemented with human bone morphogenetic protein 4 (BMP-4; 20 ng/ml;
418 Miltenyi Biotec). Three independent differentiations were done per clone.

419 Monolayer cultured hiCPC aggregates present at day 14 of the differentiation were washed with
420 MD medium, dissociated with Gentle Cell dissociation medium (Stem Cell), and centrifuged for
421 5 min at 1200 rpm. Cell aggregates were subsequently maintained in chondrogenic differentiation
422 (CD) medium containing Dulbecco's modified Eagle's medium/F12 (Gibco), supplemented with
423 1% ITS+, 55 μM 2-mercaptoethanol (Gibco), 1% non-essential amino acids (Gibco), 0.5% P/S, L-

424 ascorbate-2-phosphate (50 µg/ml; Sigma-Aldrich), L-proline (40 µg/ml; Sigma-Aldrich), ML329
425 (1µM; CSNpharm), C59 (1µM; Tocris), and transforming growth factor–β3 (10 ng/ml; PeproTech)
426 for 30 days while refreshing medium every 3 to 4 days.

427 Two different chondrogenic constructs were used for downstream analysis; these chondrogenic
428 pellets were directly used for further experiments, or they were dissociated using collagenase II,
429 encapsulated in 2% w/v agarose at 30 million cells/ml, and cultured for 14 days with CD creating
430 cylindrical shaped constructs.

431

432 *Mechanical loading*

433 The spherical shaped neo-cartilage constructs were mechanically loaded using a MACH-1
434 mechanical testing device (Biomomentum), at a rate of 5hz with 20% sinusoidal peak-to-peak
435 strain for 10 minutes as described earlier (*21*)

436

437 *sGAG measurement*

438 Sulphated glycosaminoglycan (sGAG) concentrations in the neo-cartilage organoids (µg sGAG/µg
439 DNA) was measured using the Farndale Dimethyl Methylene Blue (DMMB, Sigma) method (*36*).
440 Chondroitin sulphate (Sigma) was used as a reference standard. Absorbance was measured at 535
441 and 595 using a microplate reader (Synergy HT, Biotek). Neo-cartilage sGAG concentrations were
442 corrected for DNA content measured with the Qubit® 2.0 Fluorometer (Invitrogen™) using the
443 dsDNA HS Assay Kit (Invitrogen™).

444

445 *Histology and immunohistochemistry*

446 Neo-cartilage samples were fixed in 4% formaldehyde and embedded in paraffin. Sections were
447 stained with Alcian Blue (Sigma-Aldrich) and Nuclear Fast Red (Sigma-Aldrich). Deposition of
448 collagen II and collagen VI in the neo-cartilage constructs was visualized immunohistochemically.
449 For collagen VI, antigen retrieval was done by treating deparaffinized sections with proteinase K
450 (5 µg/ml, Qiagen) and hyaluronidase (5 mg/ml, Sigma). Sections were incubated overnight with a
451 primary antibody raised against human collagen VI (1:100, abcam), followed by incubation with
452 a HRP conjugated secondary antibody (ImmunoLogic). Peroxidase binding for collagen VI was
453 visualized using diaminobenzidine, and sections were counterstained with haematoxylin.

454

455 *RT-qPCR*

456 Per sample, two replicate neo-cartilage pellets were collected in TRIzol (Invitrogen™) and RNA
457 was isolated using the RNeasy Mini Kit (Qiagen) according to manufacturer's protocol. DNA
458 contamination was removed by treating the RNA with RNase-Free DNase RNA quality
459 (A260/280: 1.7-2.0) was assessed using the Nanodrop. RNA concentrations were measured with
460 the Qubit® 2.0 Fluorometer (Invitrogen™) using the RNA HS Assay Kit (Invitrogen™).,
461 respectively, with an A260/280 between 1.7-2.0. RNA was reverse transcribed into cDNA using
462 the Transcriptor First Strand cDNA Synthesis Kit (Roche). cDNA was amplified using FastStart
463 SYBR Green Master (Roche) and mRNA expression was measured in triplicates in a MicroAmp™
464 Optical 384-Well Reaction Plate (ThermoFisher Scientific), using the QuantStudio™ Flex Real-
465 Time PCR system (Applied Biosystems™), with the following cycling conditions: 10 min 95 °C;
466 10 sec 95 °C, 30 sec 60 °C, 20 sec 72 °C (45 cycles); 1 min 65 °C and 15 sec 95 °C . Primer

467 efficiency was tested using a cDNA dilution series, and primers were considered efficient with an
468 efficiency between 90% and 110%. -ΔCt expression levels were calculated using two
469 housekeeping genes *GAPDH* and *SDHA*, with the following formula: *ΔCt=Ct (gene of interest) –*
470 *Ct (average housekeeping genes)*. Both housekeeping genes were stably expressed in this model.
471 Fold changes were calculated using the $2^{-\Delta\Delta Ct}$ method with *ΔΔCt=ΔCt (MS) – ΔCt (Control)*.

472

473 *RNAseq*

474 RNA from neo-cartilage constructs was extracted 12 hours post mechanical loading. RNA from
475 spherical neo-cartilage constructs was extracted and processed using a pestle homogenizer in
476 TRIzol reagent (Invitrogen). RNA was extracted using chloroform, followed by precipitation using
477 ethanol, and purified with the RNeasy Mini Kit (Qiagen). Genomic DNA was removed by DNase
478 digestion (Qiagen). Paired-end 2 × 150 base pair RNA sequencing (Illumina NEBNext Ultra II
479 Directional RNA Library Prep, Illumina NOVAseq 6000) was performed. Strand-specific RNA-
480 sequencing libraries were generated which yielded on average 25 million reads per sample. Data
481 from the Illumina platform was analyzed with an in-house pipeline as previously described (*16*).
482 The adapters were clipped using Cutadapt v1.1. RNA-seq reads were then aligned using GSNAP
483 against GRCh38 (*37*). Read abundances per sample were estimated using HTSeq count v0.11.1
484 (*38*) with Ensembl gene annotation version 94. Only uniquely mapping reads were used for
485 estimating expression. The quality of the raw reads and initial processing for RNA sequencing was
486 checked using MulitQC v1.9 (*39*). Samples containing > 50% genes with zero values and average
487 read count < 4 were removed from further analysis. The datasets from both neo-cartilage models
488 were combined using surrogate variable analysis using the R package SVA version 3.42.0 (*40*).

489 Outliers where identified (n=2) using hierarchical clustering and principal component analysis
490 (PCA) which were removed from further analysis. In total, 52 samples were included of which;
491 isogenic controls (free-swelling isogenic controls=13, mechanically stimulated isogenic
492 controls=13) as well as COL6A3-mutant (free-swelling COL6A3 mutants=14 and mechanically
493 loaded COL6A3 mutants, n=12) organoids. Differential expression analysis was performed using
494 the R package DESeq version 1.34 (*41*). All samples were combined in a multifactorial analysis.
495 To determine effects of the mutation and hyper-physiological mechanical loading conditions only
496 the main effects were included into the model. To determine the interaction effect an interaction
497 term to this model was added. P-values were corrected for their false discovery rate using the
498 Benjami and Hochman method (*42*). WGCNA analysis was performed using the R package
499 WGCNA version 1.71 (*20, 43*). A generalized linear model was used to determine the association
500 between the COL6A3 mutation, hyper-physiological mechanical loading conditions, the
501 interaction effect and the identified WGCNA co-expression networks. Over representation
502 enrichment analyses of these co-expression networks using the KEGG, Reactome and gene
503 ontologie biological processes databases was performed using the anRichment R package version
504 1.22. Protein-protein network analysis was performed using the online tool STRING version 11.0
505 (*44*).

506

507 *Solid-phase binding assay*

508 Conditioned medium of wild-type and *COL6A3* mutant organoids was collected and concentrated
509 in preparation for the binding assay. To this end, 450 µl of medium was collected in 100 K
510 molecular weight cutoff Pierce Protein Concentrators (Thermo Scientific) and centrifuged for 10

511 min at 12,000g. Subsequently, COL6 concentration was determined using the Human COL6A3
512 ELISA Kit (Assay Genie) according to the manufacturer's protocol.

513 Clear multiwell plates (R&D Systems) were coated overnight with 100 µl of purified fibronectin
514 (10 µg/ml; Merck) in phosphate-buffered saline (PBS) at 4°C, followed by four wash steps with
515 wash buffer (0.05% Tween 20 in PBS). Nonspecific binding was blocked for 1 hour with 3% (w/v)
516 bovine serum albumin (BSA) in PBS. After washing with wash buffer, the plates were incubated
517 with 100 µl of concentrated medium samples at COL6A3 concentration of 1.3 ng/ml in assay
518 buffer (0.05% Tween 20 and 0.5% BSA in PBS) for 2 hours. Plates were then washed four times
519 with wash buffer and incubated with rabbit anti-COL6A3 biotin-conjugated antibody (Assay
520 Genie) at 0.2 µg/ml in assay buffer for 1 hour. Plates were washed, after which the plates were
521 incubated with streptavidin–horseradish peroxidase (Thermo Scientific) at 0.1 µg/ml in assay
522 buffer for 1 hour. After washing, color development was performed with 100 µl of
523 tetramethylbenzidine substrate (Thermo Fisher Scientific) for 10 min, reaction was stopped with
524 100 µl of 1 M HCl, and absorbance was measured at 450 nm. Assays were performed in triplicate.

525

526 *Transmission electron microscopy*

527 To the neo-cartilage organoids, consisting of cells and matrix, double concentrated fixative was
528 added to the culture medium resulting in a final concentration of 1,5% glutaraldehyde solution in
529 0,1M cacodylate buffer. The spheres were kept in fixative for at least an hour at room temperature.
530 After rinsing 3 times with 0,1M cacodylate buffer the spheres were postfixed in 1% osmium
531 tetroxide / 1,5% potassium ferricyanide / 0,1M cacodylate buffer at 4°C for an hour. After 3 times
532 rinsing with 0,1M cacodylate buffer the spheres were divided into 4 quarters. The quarters were

533 dehydrated in a series of ethanol (70%, 80%, 90% and 100%), followed by an infiltration series
534 of acetone / EPON LX112 (Ladd Research Industries) mixtures (2:1, 1:1 and 1:2), each step 30
535 min, and finally in pure EPON LX 112 for 1 hour. The quarters were positioned in a mold with
536 the wide side towards the cutting surface, filled up with EPON and put in an 70 °C oven to
537 polymerize for 48 hours.

538 Ultrathin sections (90 nm) were made with a Leica EM UC6 ultramicrotome and collected on 50
539 mesh grids. Sections were stained with 7% uranyl acetate in MilliQ for 10 minutes and lead citrate
540 (*45*). Sections were then imaged in a Tecnai T12 twin (FEI / Thermo Fisher Scientific) with a
541 Gatan 4kx4k OneView camera (Gatan) at 21.000x magnification (at a pixel size of 1.03 nm) for
542 machine learning analysis using automated tiled imaging (MyTEM) and images were stitched
543 together into virtual slides (MyStitch) (*46*).

544

545 *Image Analysis*

546 For image analysis, in total 18 virtual slides were used from three isogenic control and three
547 *COL6A3* mutant neo-cartilage organoids (3 positions each). Using a custom-written user interface
548 software (to be published) GAG structures were manually annotated in both control and mutated
549 samples and from this a model was trained for machine learning. The structures were predicted in
550 all 18 slides (Fig. S5). Both the surface of the GAGs and their number was extracted from the
551 predictions.

552

553 *Statistical analysis*

554 For all data analysis except RNA sequencing we have used a generalized linear model including
555 the factors hyper-physiological loading and the *COL6A3* mutation using R statistical software
556 version 4.1.1.

557

558 **References**

559 1. F. Guilak, Biomechanical factors in osteoarthritis. *Best Pract Res Clin Rheumatol* **25**,
560 815-823 (2011).
561 2. C. Juhl, R. Christensen, E. M. Roos, W. Zhang, H. Lund, Impact of exercise type and
562 dose on pain and disability in knee osteoarthritis: a systematic review and meta-
563 regression analysis of randomized controlled trials. *Arthritis Rheumatol* **66**, 622-636
564 (2014).
565 3. O. A. Uthman, D. A. van der Windt, J. L. Jordan, K. S. Dziedzic, E. L. Healey, G. M.
566 Peat, N. E. Foster, Exercise for lower limb osteoarthritis: systematic review incorporating
567 trial sequential analysis and network meta-analysis. *BMJ* **347**, f5555 (2013).
568 4. S. A. Olson, F. J. P. Guilak, Post-traumatic Arthritis. (2015).
569 5. F. Guilak, R. J. Nims, A. Dicks, C. L. Wu, I. Meulenbelt, Osteoarthritis as a disease of
570 the cartilage pericellular matrix. *Matrix Biol* **71-72**, 40-50 (2018).
571 6. N. A. Zelenski, H. A. Leddy, J. Sanchez-Adams, J. Zhang, P. Bonaldo, W. Liedtke, F.
572 Guilak, Type VI Collagen Regulates Pericellular Matrix Properties, Chondrocyte
573 Swelling, and Mechanotransduction in Mouse Articular Cartilage. *Arthritis Rheumatol*
574 **67**, 1286-1294 (2015).
575 7. F. Guilak, L. G. Alexopoulos, M. L. Upton, I. Youn, J. B. Choi, L. Cao, L. A. Setton, M.
576 A. Haider, The pericellular matrix as a transducer of biomechanical and biochemical
577 signals in articular cartilage. *Ann N Y Acad Sci* **1068**, 498-512 (2006).
578 8. L. G. Alexopoulos, I. Youn, P. Bonaldo, F. Guilak, Developmental and osteoarthritic
579 changes in Col6a1-knockout mice: biomechanics of type VI collagen in the cartilage
580 pericellular matrix. *Arthritis Rheum* **60**, 771-779 (2009).
581 9. C. G. Bonnemann, The collagen VI-related myopathies: muscle meets its matrix. *Nat Rev*
582 *Neurol* **7**, 379-390 (2011).
583 10. N. Beecher, A. M. Roseman, T. A. Jowitt, R. Berry, H. Troilo, R. A. Kammerer, C. A.
584 Shuttleworth, C. M. Kielty, C. Baldock, Collagen VI, conformation of A-domain arrays
585 and microfibril architecture. *J Biol Chem* **286**, 40266-40275 (2011).
586 11. C. Wiberg, A. R. Klatt, R. Wagener, M. Paulsson, J. F. Bateman, D. Heinegard, M.
587 Morgelin, Complexes of matrilin-1 and biglycan or decorin connect collagen VI
588 microfibrils to both collagen II and aggrecan. *J Biol Chem* **278**, 37698-37704 (2003).
589 12. U. Specks, U. Mayer, R. Nischt, T. Spissinger, K. Mann, R. Timpl, J. Engel, M. J. T. E. j.
590 Chu, Structure of recombinant N-terminal globule of type VI collagen alpha 3 chain and
591 its binding to heparin and hyaluronan. **11**, 4281-4290 (1992).
592 13. M. van Hoolwerff, A. Rodriguez Ruiz, M. Bouma, H. E. D. Suchiman, R. I. Koning, C.
593 R. Jost, A. A. Mulder, C. Freund, F. Guilak, Y. F. M. Ramos, I. Meulenbelt, High-impact

FN1 mutation decreases chondrogenic potential and affects cartilage deposition via decreased binding to collagen type II. *Sci Adv* **7**, eabg8583 (2021).

14. N. Riyazi, F. R. Rosendaal, E. Slagboom, H. M. Kroon, F. C. Breedveld, M. Kloppenburg, Risk factors in familial osteoarthritis: the GARP sibling study. *Osteoarthritis Cartilage* **16**, 654-659 (2008).
15. A. Kiezun, S. L. Pulit, L. C. Francioli, F. van Dijk, M. Swertz, D. I. Boomsma, C. M. van Duijn, P. E. Slagboom, G. J. van Ommen, C. Wijmenga, C. Genome of the Netherlands, P. I. de Bakker, S. R. Sunyaev, Deleterious alleles in the human genome are on average younger than neutral alleles of the same frequency. *PLoS Genet* **9**, e1003301 (2013).
16. R. Coutinho de Almeida, Y. F. M. Ramos, A. Mahfouz, W. den Hollander, N. Lakenberg, E. Houtman, M. van Hoolwerff, H. E. D. Suchiman, A. Rodriguez Ruiz, P. E. Slagboom, H. Mei, S. M. Kielbasa, R. Nelissen, M. Reinders, I. Meulenbelt, RNA sequencing data integration reveals an miRNA interactome of osteoarthritis cartilage. *Ann Rheum Dis* **78**, 270-277 (2019).
17. G. N. Welch, J. J. N. E. j. o. m. Loscalzo, Homocysteine and atherothrombosis. **338**, 1042-1050 (1998).
18. D. A. Keesler, T. L. Slobodianuk, C. E. Kochelek, C. W. Skaer, S. L. Haberichter, V. H. Flood, Fibronectin binding to von Willebrand factor occurs via the A1 domain. *Res Pract Thromb Haemost* **5**, e12534 (2021).
19. S. S. Adkar, C. L. Wu, V. P. Willard, A. Dicks, A. Ettyreddy, N. Steward, N. Bhutani, C. A. Gersbach, F. Guilak, Step-Wise Chondrogenesis of Human Induced Pluripotent Stem Cells and Purification Via a Reporter Allele Generated by CRISPR-Cas9 Genome Editing. *Stem Cells* **37**, 65-76 (2019).
20. B. Zhang, S. J. S. a. i. g. Horvath, m. biology, A general framework for weighted gene co-expression network analysis. **4**, (2005).
21. R. G. M. Timmermans, N. G. C. Bloks, M. Tuerlings, M. van Hoolwerff, R. G. H. H. Nelissen, R. J. P. van der Wal, P. M. van der Kraan, A. B. Blom, M. H. J. van den Bosch, Y. F. M. Ramos, I. Meulenbelt, A human in vitro 3D neo-cartilage model to explore the response of OA risk genes to hyper-physiological mechanical stress. *Osteoarthritis and Cartilage Open* **4**, (2022).
22. R. J. Nims, L. Pferdehirt, N. B. Ho, A. Savadipour, J. Lorentz, S. Sohi, J. Kassab, A. K. Ross, C. J. O'Conor, W. B. J. S. A. Liedtke, A synthetic mechanogenetic gene circuit for autonomous drug delivery in engineered tissues. **7**, eabd9858 (2021).
23. L. S. Simon, Role and regulation of cyclooxygenase-2 during inflammation. *The American journal of medicine* **106**, 37S-42S (1999).
24. F. Guo, Y. Li, S. J. I. Wu, Antisense IRAK-2 Oligonucleotide Blocks Il-1-Stimulated NF-κB Activation and ICAM-1 Expression in Cultured Endothelial Cells. **23**, 535-543 (1999).
25. T. L. Vincent, Mechanoflammation in osteoarthritis pathogenesis. *Semin Arthritis Rheum* **49**, S36-S38 (2019).
26. S. Wu, D. Fadoju, G. Rezvani, F. De Luca, Stimulatory effects of insulin-like growth factor-I on growth plate chondrogenesis are mediated by nuclear factor-kappaB p65. *J Biol Chem* **283**, 34037-34044 (2008).
27. S. Wu, J. K. Flint, G. Rezvani, F. J. J. o. B. C. De Luca, Nuclear factor-κB p65 facilitates longitudinal bone growth by inducing growth plate chondrocyte proliferation and differentiation and by preventing apoptosis. **282**, 33698-33706 (2007).

640 28. E. Houtman, M. Tuerlings, J. Riechelman, E. Suchiman, R. J. P. van der Wal, R.
641 Nelissen, H. Mei, Y. F. M. Ramos, R. Coutinho de Almeida, I. Meulenbelt, Elucidating
642 mechano-pathology of osteoarthritis: transcriptome-wide differences in mechanically
643 stressed aged human cartilage explants. *Arthritis Res Ther* **23**, 215 (2021).
644 29. A. Burleigh, A. Chanalaris, M. D. Gardiner, C. Driscoll, O. Boruc, J. Saklatvala, T. L.
645 Vincent, Joint immobilization prevents murine osteoarthritis and reveals the highly
646 mechanosensitive nature of protease expression in vivo. *Arthritis Rheum* **64**, 2278-2288
647 (2012).
648 30. L. Puljak, A. Marin, D. Vrdoljak, F. Markotic, A. Utrobicic, P. Tugwell, Celecoxib for
649 osteoarthritis. *Cochrane Database Syst Rev* **5**, CD009865 (2017).
650 31. H. Miyoshi, K. L. VanDussen, N. P. Malvin, S. H. Ryu, Y. Wang, N. M. Sonnek, C. W.
651 Lai, T. S. Stappenbeck, Prostaglandin E2 promotes intestinal repair through an adaptive
652 cellular response of the epithelium. *EMBO J* **36**, 5-24 (2017).
653 32. C. J. O'Conor, H. A. Leddy, H. C. Benefield, W. B. Liedtke, F. Guilak, TRPV4-mediated
654 mechanotransduction regulates the metabolic response of chondrocytes to dynamic
655 loading. *Proc Natl Acad Sci U S A* **111**, 1316-1321 (2014).
656 33. M. R. Servin-Vences, M. Moroni, G. R. Lewin, K. Poole, Direct measurement of TRPV4
657 and PIEZO1 activity reveals multiple mechanotransduction pathways in chondrocytes.
658 *Elife* **6**, (2017).
659 34. W. J. Kent, C. W. Sugnet, T. S. Furey, K. M. Roskin, T. H. Pringle, A. M. Zahler, D. J.
660 G. r. Haussler, The human genome browser at UCSC. **12**, 996-1006 (2002).
661 35. A. Rodriguez Ruiz, A. Dicks, M. Tuerlings, K. Schepers, M. van Pel, R. Nelissen, C.
662 Freund, C. L. Mummery, V. Orlova, F. Guilak, I. Meulenbelt, Y. F. M. Ramos, Cartilage
663 from human-induced pluripotent stem cells: comparison with neo-cartilage from
664 chondrocytes and bone marrow mesenchymal stromal cells. *Cell Tissue Res* **386**, 309-320
665 (2021).
666 36. R. W. Farndale, C. A. Sayers, A. J. Barrett, A Direct Spectrophotometric Microassay for
667 Sulfated Glycosaminoglycans in Cartilage Cultures. *Connective Tissue Research* **9**, 247-
668 248 (1982).
669 37. T. D. Wu, C. K. Watanabe, GMAP: a genomic mapping and alignment program for
670 mRNA and EST sequences. *Bioinformatics* **21**, 1859-1875 (2005).
671 38. S. Anders, P. T. Pyl, W. Huber, HTSeq--a Python framework to work with high-
672 throughput sequencing data. *Bioinformatics* **31**, 166-169 (2015).
673 39. P. Ewels, M. Magnusson, S. Lundin, M. Kaller, MultiQC: summarize analysis results for
674 multiple tools and samples in a single report. *Bioinformatics* **32**, 3047-3048 (2016).
675 40. J. T. Leek, svaseq: removing batch effects and other unwanted noise from sequencing
676 data. *Nucleic Acids Res* **42**, (2014).
677 41. M. I. Love, W. Huber, S. Anders, Moderated estimation of fold change and dispersion for
678 RNA-seq data with DESeq2. *Genome Biol* **15**, 550 (2014).
679 42. <Benjamini, Hochberg, Society - 2018 - Controlling the False Discovery Rate A Practical
680 and Powerful Approach to Multiple Testing Author.pdf>.
681 43. P. Langfelder, S. J. B. b. Horvath, WGCNA: an R package for weighted correlation
682 network analysis. **9**, 1-13 (2008).
683 44. D. Szklarczyk, A. L. Gable, D. Lyon, A. Junge, S. Wyder, J. Huerta-Cepas, M.
684 Simonovic, N. T. Doncheva, J. H. Morris, P. J. N. a. r. Bork, STRING v11: protein–

685 protein association networks with increased coverage, supporting functional discovery in
686 genome-wide experimental datasets. **47**, D607-D613 (2019).
687 45. E. J. J. C. B. Reynolds, Thc use ol lead Citrate at high pH as an electron-opaque stain in
688 electron microscopy. **17**, 20&-212 (1963).
689 46. F. G. Faas, M. C. Avramut, B. M. van den Berg, A. M. Mommaas, A. J. Koster, R. B.
690 Ravelli, Virtual nanoscopy: generation of ultra-large high resolution electron microscopy
691 maps. *J Cell Biol* **198**, 457-469 (2012).

692

693 **Acknowledgments**

694 **Funding:** Leiden University Medical Centre, Pfizer Groton, Connecticut, USA and the Dutch
695 Arthritis Society have supported the GARP study. Furthermore, the research leading to these
696 results has received funding from the Biobanking and BioMolecular resources Research
697 Infrastructure the Netherlands (BBMRI-NL) (complementation project CP2013-84), the Dutch
698 Scientific Research council NWO/ZonMW VICI scheme (nr. 91816631/528) and the Dutch
699 Arthritis Society. We are indebted to drs. N. Riyazi, J. Bijsterbosch, H.M. Kroon and I. Watt for
700 collection of data. Furthermore, this work was supported by the Shriners Hospitals for Children
701 and the NIH (grants AG46927, AG15768, AR080902, AR072999, AR073752, and AR074992).
702 Additionally, the data is generated within the scope of the Medical Delta programs Regenerative
703 Medicine 4D: Generating complex tissues with stem cells and printing technology and Improving
704 Mobility with Technology.

705

706 **Author Contributions:** N.G.C.B., Z.H., A.R.D., Y.F.M.H, F.G., I.M. developed the concept of
707 this study; N.G.C.B., Z.H., S.S.A., A.R.D., G.H., N.S. M.K., R.I.K., A.A.M., B.B.R.K. and F.G.,
708 acquired materials and data; N.G.C.B., R.C.D.A., B.B.R.K., Y.F.M.H, F.G. and I.M. analyzed the
709 data; and all authors contributed to the writing of the manuscript.

710 **Competing interests:** F.G. is an employee and shareholder in Cytex Therapeutics Inc. The authors
711 declare that they have no other competing interests.

712 **Data and materials availability:** All data needed to evaluate the conclusions in the paper are
713 present in the paper and/or the Supplementary Materials.

714

715 **Figures and Tables**

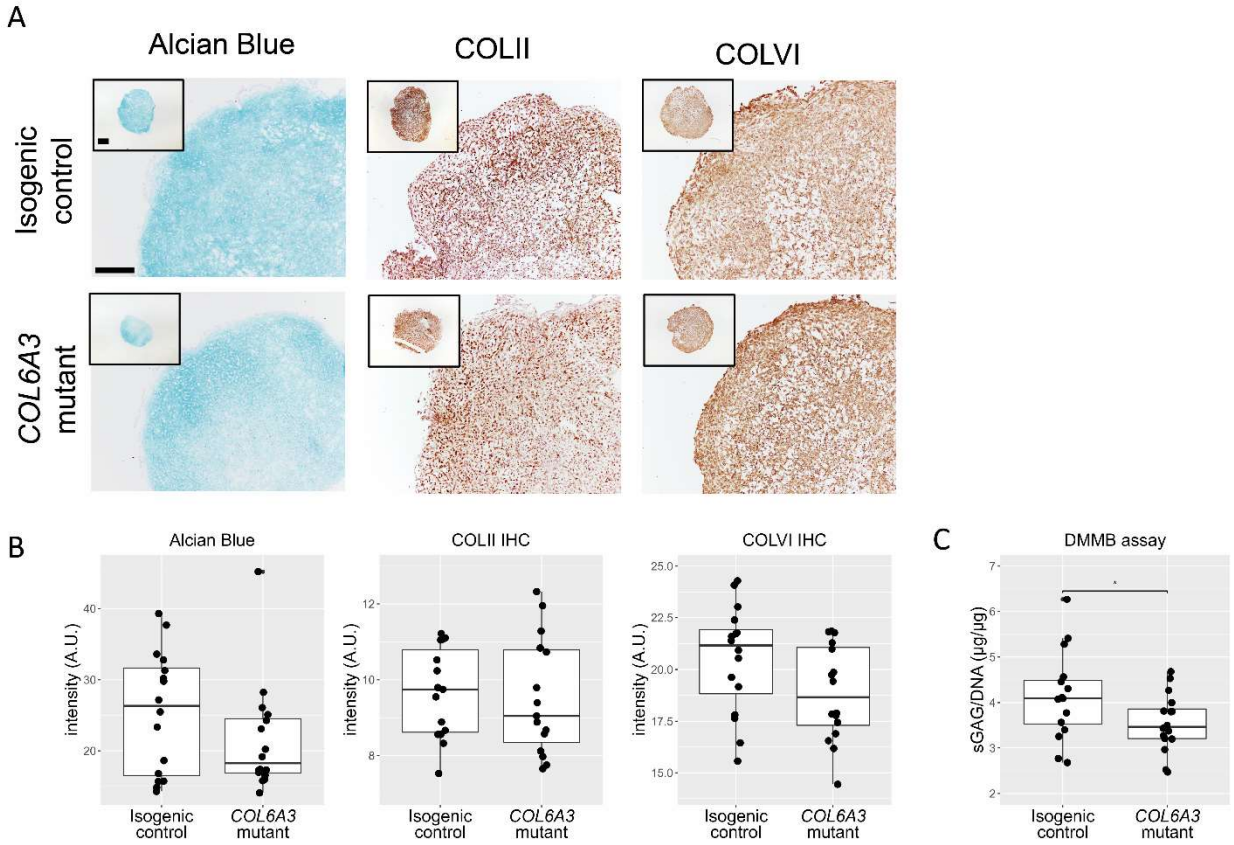

716

717 **Figure 1. Effect of the mutation on neo-cartilage matrix deposition. (A)** Representative images
718 of Alcian blue staining marking sulfated glycosaminoglycans (sGAGs) and immunohistological
719 staining of collagen II (COL II) and collagen VI (COLVI). Scale bar 200µm. **(B)** Quantification
720 of Alcian blue, COLII, and COLVI in isogenic control and *COL6A3*-mutant neo-cartilage
721 organoids showed no significant effect of the mutation (N=16). **(C)** Quantification of sGAG
722 deposition in neo-cartilage organoids. sGAG deposition in COLVI-mutant neo-cartilage organoids
723 is reduced in comparison to isogenic controls (beta=0.55 ± 0.28, P=4.9x10^{-2}, N=16). Statistics are
724 reported as beta ± standard error. The box plots represent 25th, 50th, and 75th percentiles, and
725 whiskers extend to 1.5 times the interquartile range. Individual samples are depicted by black dots

726 in each graph. P values were attained using a generalized linear model with intensity (for immuno-
727 stainings) and (sGAGs/DNA) as dependent variable and genotype as independent variable.

728

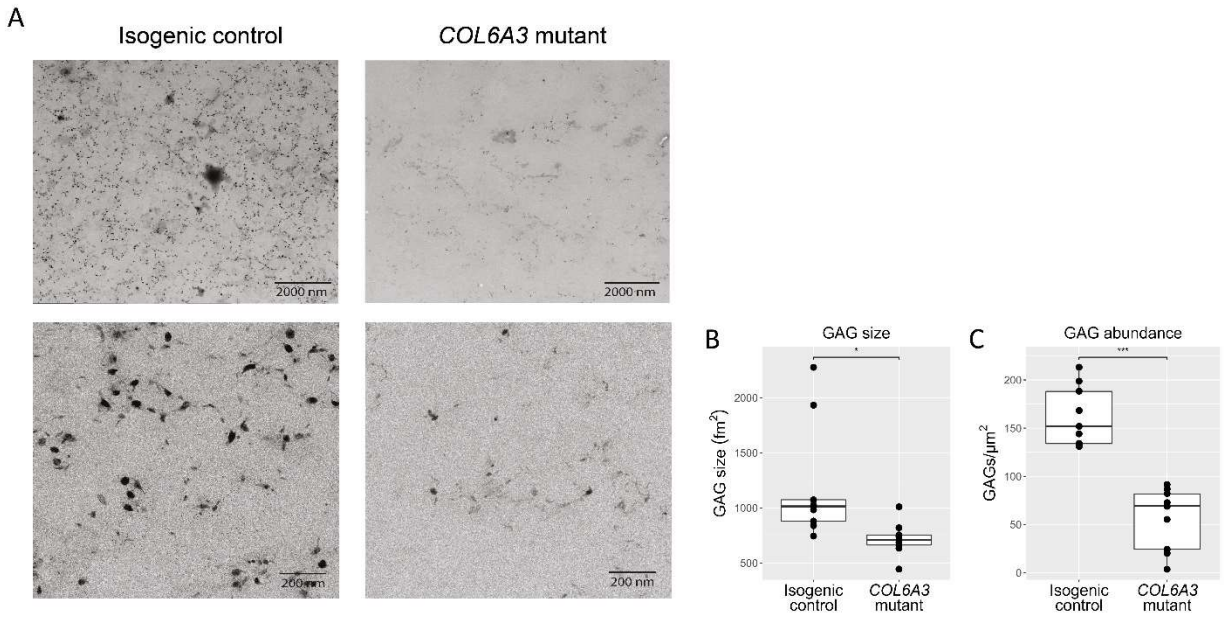

729

730 **Figure 2. The COLVI mutation reduces sGAG aggregate size. (A)** TEM image of isogenic
731 control (left) and a *COL6A3*-mutant (right) neo-cartilage organoid. **(B)** Using a deep-learning
732 algorithm, the sGAG aggregate size was measured, showed a reduction in the *COL6A3*-mutant
733 neo-cartilage organoids (beta=-479.7, $P=1.93X10^{-2}$). **(C)** GAG amount was decreased in the
734 *COL6A3*-mutant neo-cartilage organoids (beta=-106.14 ± 14.95, $P=2.52X10^{-6}$). Statistics are
735 reported as beta ± standard error. The box plots represent 25th, 50th, and 75th percentiles, and
736 whiskers extend to 1.5 times the interquartile range. Individual samples are depicted by black dots
737 in each graph. P values were attained using a generalized linear model, with GAG size or
738 $GAGs/mm^2$ as a dependent variable and genotype as an independent variable.

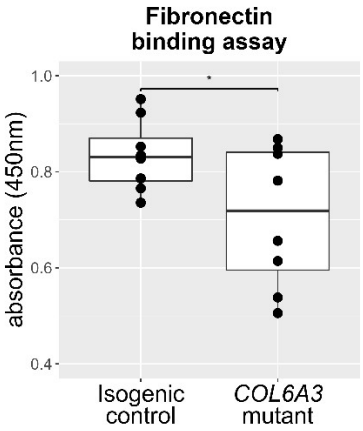

739

740 **Figure 3. The COLVI mutation reduces binding to fibronectin (A)** Solid-phase binding assay
741 with full-length fibronectin-coated wells and wild-type and R1504W mutant COLVI. R1504W
742 showed a reduced binding to fibronectin (beta=-0.13 ± 0.06, P=4.37 x10^{-2}, N=8). This assay did
743 not show binding of COLVI to hyaluronan. Statistics are reported as beta ± standard error. The
744 box plots represent 25th, 50th, and 75th percentiles, and whiskers extend to 1.5 times the
745 interquartile range. Individual samples are depicted by black dots in each graph. P values were
746 attained using a generalized linear model with absorbance at 450nm as dependent variable and
747 genotype as independent variable.

748

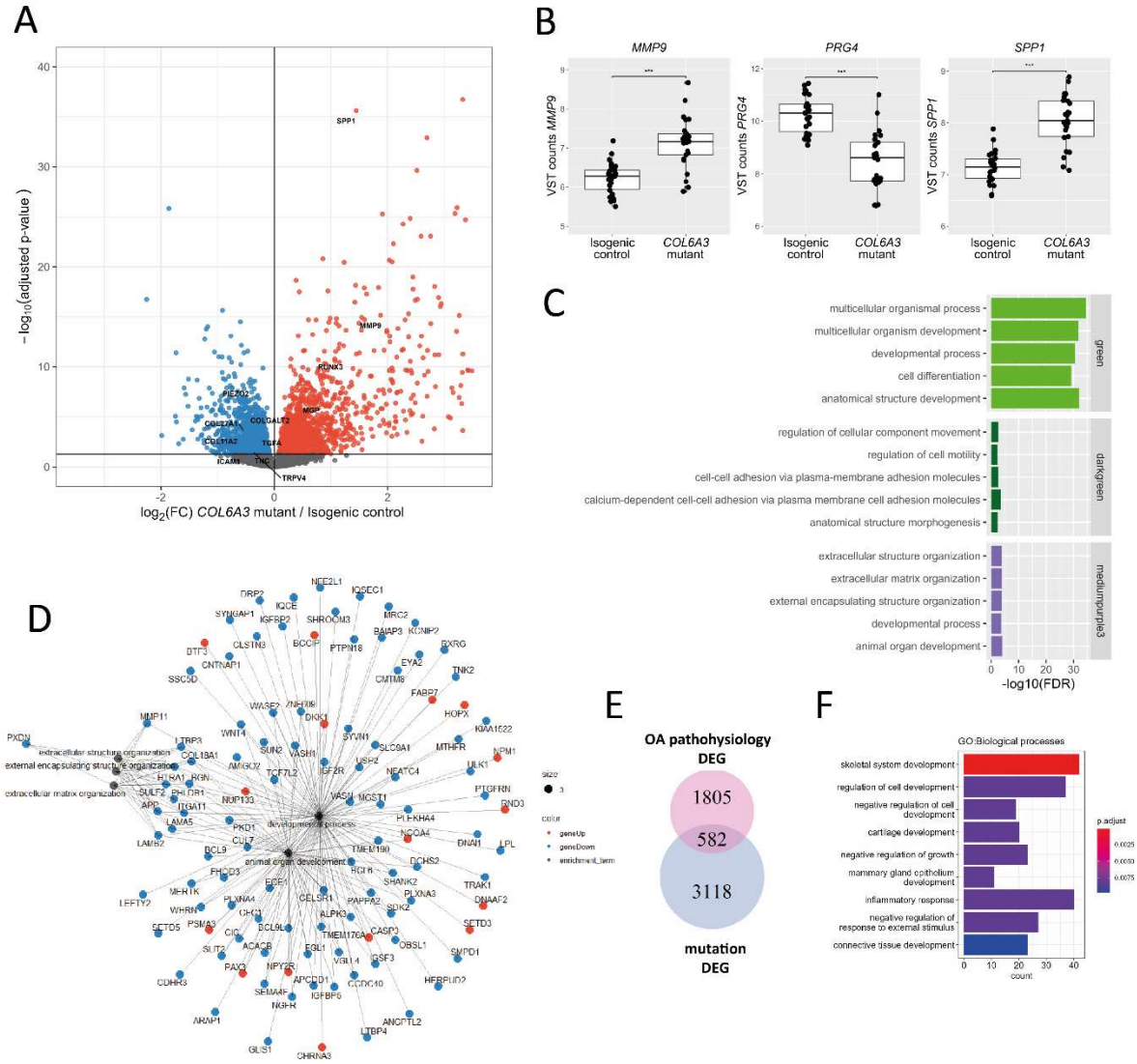

Figure 4. Transcriptomic profile in presence of the *COL6A3* mutation (A) Volcano plot showing the differentially expressed genes (DEGs) in response to the *COL6A3* mutation (N=26). Red dots denote DEGs with an FDR<0.05 that are upregulated, and blue dots represent DEGs that are downregulated, as determined by DESeq2 analysis. **(B)** Notable examples of DEGs between isogenic control and *COL6A3*-mutant neo-cartilage pellets. The box plots represent 25th, 50th, and 75th percentiles, and whiskers extend to 1.5 times the interquartile range. Individual samples are depicted by black dots in each graph. ***FDR<0.001 **(C)** Overrepresentation enrichment analysis (KEGG, REACTOME, GO biological processes) of the top 3 weighted gene co-expression

network analysis (WGCNA) co-expression modules where the first principal component is significantly associated with the *COL6A3* mutation. **(D)** Pathway – gene network of the enrichment analysis of the mediumpurple3 cluster. Lines depict the relationship between the genes and the pathways determined by enrichment analysis. Blue dots depict downregulated DEGs with the *COL6A3* mutation, while red dots depict upregulated DEGs with the *COL6A3* mutation. **(E)** Overlap between the *COL6A3* mutation DEGs and differential expression between lesioned and preserved cartilage from a previously published dataset (RAAK study, Ramos et al., 2014). **(F)** Over-representation enrichment analysis of overlapping DEGs between the mutation and lesioned versus preserved cartilage. Count depicts the number of genes that are categorized to each pathway.

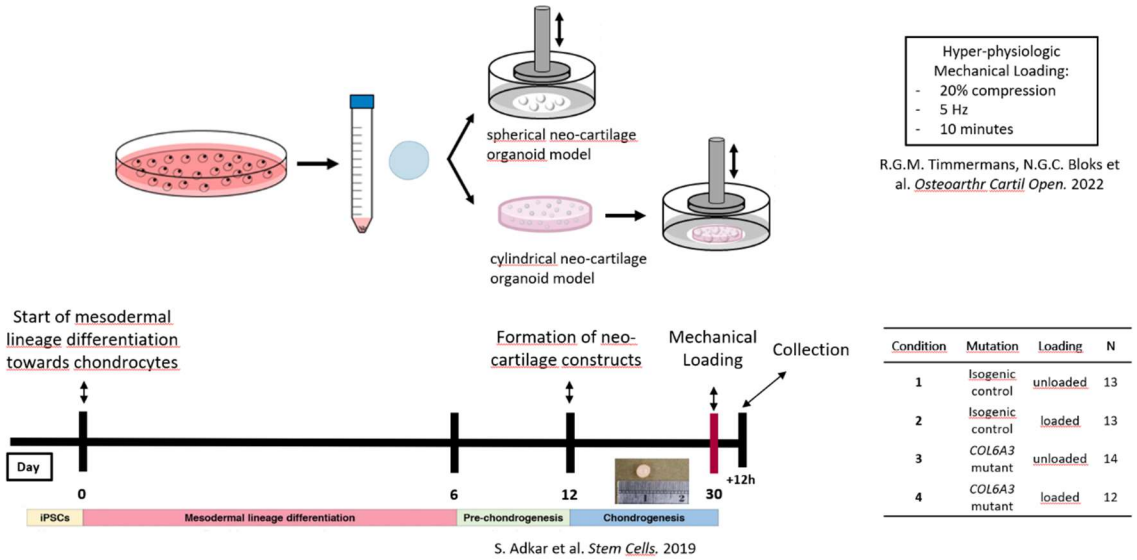

Condition	Mutation	Loading	N
1	Isogenic control	unloaded	13
2	Isogenic control	loaded	13
3	*COL6A3* mutant	unloaded	14
4	*COL6A3* mutant	loaded	12

Figure 5. Chondrogenic models to study the effects of aberrant COLVI function in interaction with hyper-physiologic mechanical loading conditions. hiPSCs in which the

R1504W mutation was introduced using CRISPR-Cas9 genome editing. These cells were differentiated using an established differentiation protocol to produce neo-cartilage organoids. Two different organoid models were employed; 1. A spherical pellet model harnessing the original matrix produced by the hiPSCs. 2. A cylindrical organoid model in which the hiPSc-derived chondrocytes were embedded in an agarose construct, ideally suited for testing the effects of mechanical loading conditions. These constructs were both exposed to hyper-physiological loading conditions, after which the organoids were harvested for downstream analysis.

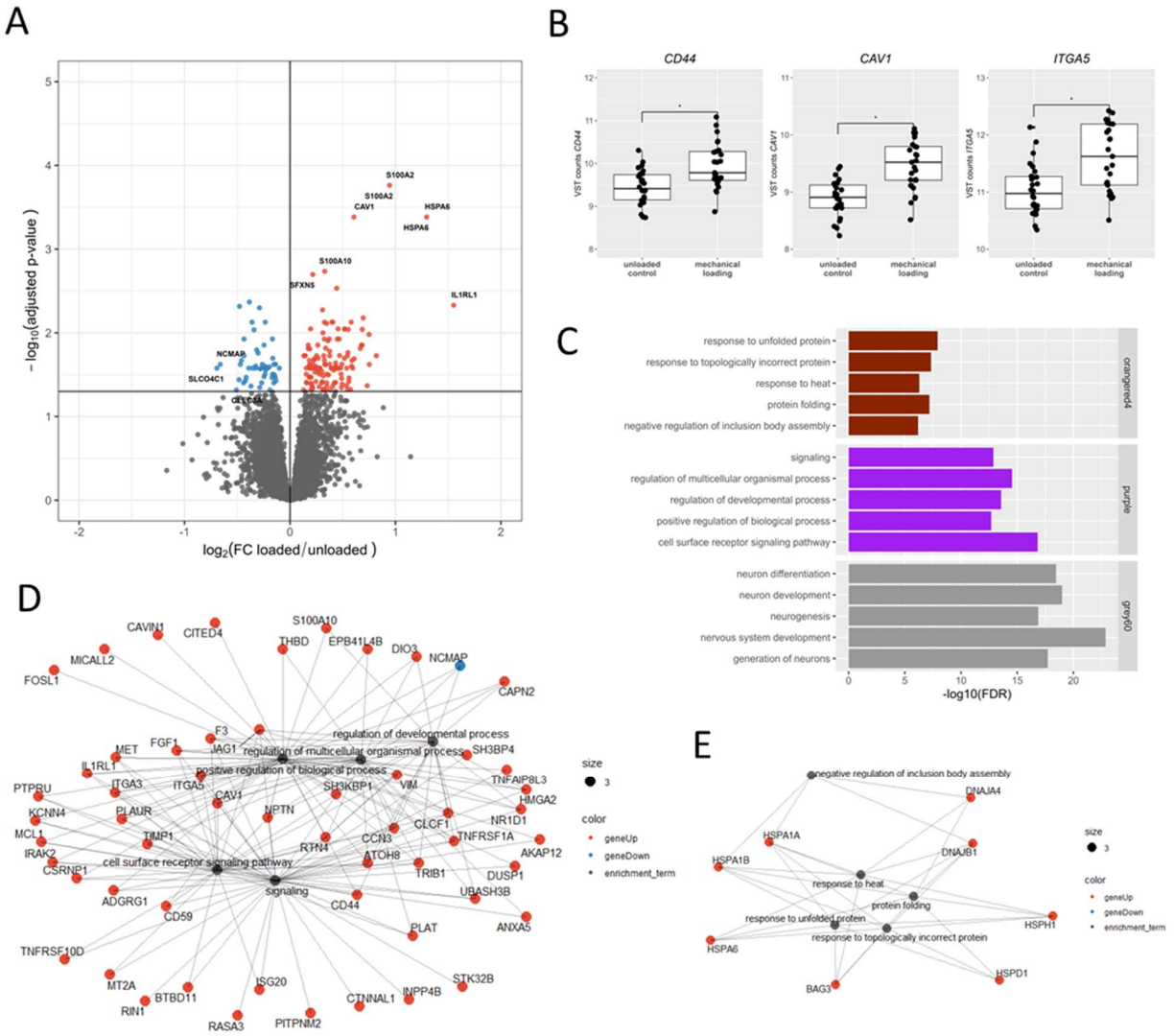

779 **Figure 6. Transcriptomic profile in response to hyper-physiologic mechanical loading**
780 **conditions. (A)** Volcano plot of differentially expressed genes (DEGs) in response to hyper-
781 physiologic loading conditions. Red dots denote differentially DEGs with an FDR<0.05 that are
782 upregulated, and blue dots represent DEGs that are downregulated as determined by DESeq2
783 analysis. **(B)** Notable examples of mechano-sensor genes upregulated in response to hyper-
784 physiological mechanical loading conditions. The box plots represent the 25th, 50th, and 75th
785 percentiles, and the whiskers extend to 1.5 times the interquartile range. Individual samples are
786 depicted by black dots in each graph. *FDR<0.05 **(C)** Overrepresentation enrichment analysis
787 (KEGG, REACTOME, GO biological processes) of the top 3 weighted gene co-expression
788 network analysis (WGCNA) co-expression modules of which the first principle component is
789 significantly associated with hyper-physiologic mechanical loading conditions. **(D-E)** Gene-
790 pathway network of the enrichment analysis of the purple **(D)** and the orangered4 **(E)** co-
791 expression network where lines depict the relationship between the genes and the pathways
792 determined by enrichment analysis. Blue dots depict downregulated DEGs in response to hyper-
793 physiologic mechanical loading conditions, red dots depict upregulated DEGs in response to
794 hyper-physiologic mechanical loading conditions.

795

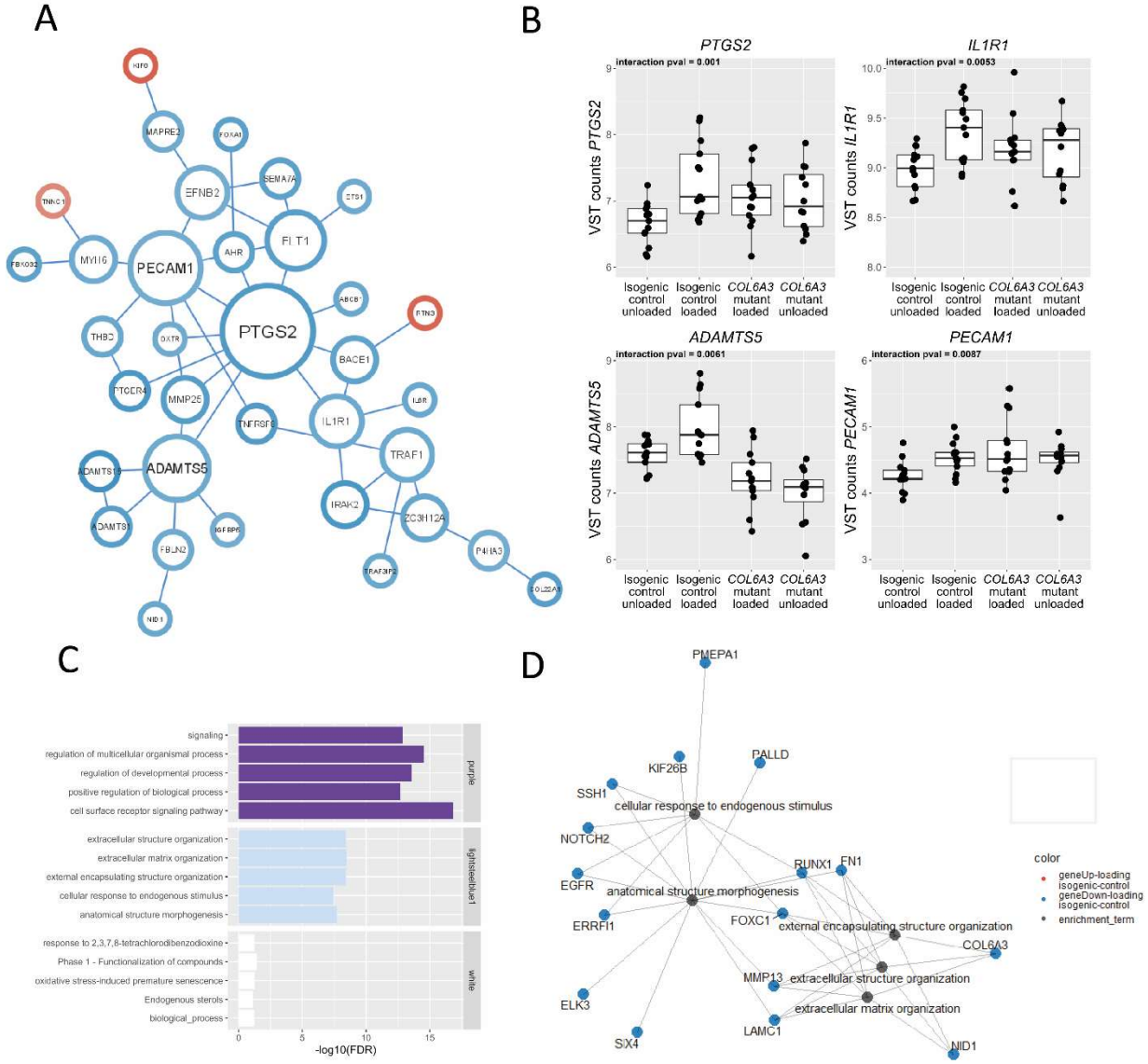

Figure 7. The *COL6A3* mutation affects the biological response to hyper-physiologic loading conditions. **(A)** Protein-protein interaction (PPI) network based on the STRING-DB of genes that show an interaction (P<0.01) between the *COL6A3* mutation and hyper-physiological mechanical loading conditions. Red circles denote an increased response to hyper-physiological mechanical loading due to the *COL6A3* mutation, while blue circles denote a reduced response to mechanical stress due to the *COL6A3* mutation (only showing connected nodes). Relative node size depicts number of connections for each gene within the network **(B)** Examples of central DEGs in the PPI

804 that are related to an inflammatory response. The box plots represent 25th, 50th, and 75th
805 percentiles, and whiskers extend to 1.5 times the interquartile range. Individual samples are
806 depicted by black dots in each graph. **(C)** Gene enrichment analysis of WGCNA hubs significantly
807 related to the interaction between the *COL6A3* mutation and the response to hyper-physiological
808 mechanical loading conditions. **(D)** Pathway – gene network of the enrichment analysis of the
809 purple cluster. Lines depict the relationship between the genes and the pathways determined by
810 enrichment analysis. Blue and red dots depict, respectively, downregulated and upregulated DEGs
811 in response to hyper-physiological loading conditions in the isogenic control neo-cartilage
812 organoids.

813

814 **Table 1. Effect of the *COL6A3* mutation on markers of cartilage metabolism**

	Effect of *COL6A3* genotype		
Gene	**beta**	**SE**	***p*-value**
Catabolic			
MMP13	0.02	0.27	0.94
MMP3	-1.19	0.70	0.09
ADAMTS5	-1.01	0.14	**<0.001**
Anabolic			
COL2A1	-0.47	0.20	**0.02**
ACAN	-0.54	0.21	**0.01**
Hypertrophic			
COL10A1	-0.07	0.16	0.65

815